2009

Numerical modeling of alpha-particle deposition in a field reversed configuration

Nilesh B. Dhote

NUMERICAL MODELING OF ALPHA-PARTICLE DEPOSITION IN A FIELD REVERSED CONFIGURATION

by

NILESH B. DHOTE

A THESIS

Submitted in partial fulfillment of the requirements
for the degree of Master of Science
in
The Department of Physics
to
The School of Graduate Studies
of
The University of Alabama in Huntsville

HUNTSVILLE, ALABAMA

2009

In presenting this thesis in partial fulfillment of the requirements for a master's degree from The University of Alabama in Huntsville, I agree that the library of this University shall make it freely available for inspection. I further agree that permission for extensive copying for scholarly purposes may be granted by my advisor or, in his/her absence, by the Chair of the Department or the Dean of the School of Graduate Studies. It is also understood that due recognition shall be given to me and to The University of Alabama in Huntsville in any scholarly use which may be made of material in this thesis.

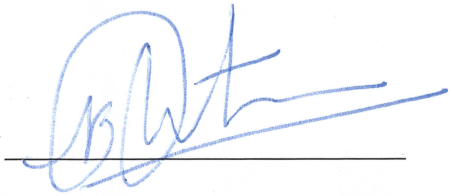

(student signature)

03/13/05

(date)

THESIS APPROVAL FORM

Submitted by Nilesh B. Dhote in partial fulfillment of the requirements for the degree of Master of Science in Physics (Optics and Photonics Technology) and accepted on behalf of the Faculty of the School of Graduate Studies by the thesis committee.

We, the undersigned members of the Graduate Faculty of the University of Alabama in Huntsville, certify that we have advised and/or supervised the candidate on the work described in this thesis. We further certify that we have reviewed the thesis manuscript and approve it in partial fulfillment of the requirements for the degree of Master of Science in Physics.

3/13/07 Committee Chair
Dr. James Miller
(Date)

3/12/09
Dr. Jason T. Cassibry

3/12/09
Dr. Don Gregory

3/13/09 Department Chair
Dr. James Miller

3/13/09 College Dean
Dr. John Fix

5/1/09 Graduate Dean
Dr. Debra M. Moriarity

ABSTRACT

The School of Graduate Studies
The University of Alabama in Huntsville

Degree Master of Science College/Dept. Science/Physics
Name of Candidate Nilesh B. Dhote
Title Numerical Modeling of Alpha Particle Deposition in Field Reversed Configuration

We present a particle model to calculate fractional alpha deposition for field reversed configuration (FRC) targets, which is important for estimation of the ignition parameter space for magnetoinertial fusion. For either high densities or high magnetic fields, the fractional deposition asymptotically approaches 1. In the low magnetic field, low density limit, the fractional deposition was linear with density. Deposition rises sharply with magnetic field between these two extremes.

The ignition region was studied using Lindl-Widner diagrams. We found that the alpha Larmor radius has to be small compared with the target radius for ignition. The ignition space peaks for a target to Larmor radius ratio of ~10. Our model can be used as a basis for further development of deposition models for other targets. Additional insights can be gained with further exploration of the ignition space with Lindl-Widner diagrams using our alpha deposition model.

Abstract Approval: Committee Chair [signature] 3/13/09
(Date)

Department Chair [signature] 3/13/09

Graduate Dean [signature] 5/1/09

ACKNOWLEDGMENTS

First of all, I would like to thank my thesis advisor, Dr. Jason Cassibry. Without him this task could not have been accomplished. I owe him a lot for giving me the chance to be a part of his research group. He was there every time I needed his help. Without his motivation and his help, I could not have accomplished this task. He truly has been an inspiration for me in my academic life.

I next would like to thank my academic advisor, Dr. Don Gregory. Radiometry, under him was the most amazing class I had at UAH. I learned a lot with the practical problems he used to give in the class.

I also would like to thank Dr. James Miller, Chair of the Physics Department, for chairing my committee.

I thank physics department secretary Dora Wynn, and PRC staff member Deborah Boglin for being so kind to me and helping me out with all kinds of paperwork.

I would also like to thank Seth Thompson. Each time I would go to him to ask about any problem, he would always come up with more than one way to approach and solve that problem.

I thank Ravi Paul Golapalli, Kiranmayee Kilaru, Dr. John Sinko, Coby McColgin, Kjell Edmund Ims, Dr. Valentin Korman of K Sciences, for their help. I also thank Yao Wang for helping me out in formatting.

I would like to thank all my friends for being supportive during my writing.
And above all, I owe so much to my family, and my brother for their overwhelming love, support, and patience. My father has always been a source of inspiration for me, and my mother made many sacrifices so that I could complete my education.

Finally, I thank the Lord for giving me the strength and courage to overcome life's obstacles.

TABLE OF CONTENTS

Page

LIST OF FIGURES

Figure Page

LIST OF TABLES

Table Page

CHAPTER 1

INTRODUCTION

The primary objective of this thesis is to estimate the fractional alpha particle energy deposition for field reversed configuration (FRC) targets. We are motivated by the interest in determining realistic ignition conditions for magnetoinertial fusion (MIF) [1]. The FRC magnetic topology is considered because of its ability for high plasma beta, the ratio of the hydrodynamic pressure to the magnetic field pressure [2]. Below we discuss the basics of alpha particle motion in a bath of colder plasma, which is necessary for understanding the physics of deposition. We then provide an overview of nuclear fusion.

1.1. Basics of Alpha Particle Motion

The motion of a charged particle in the presence of a steady magnetic field and collisions can be described classically by a statement of Newton's second law

$$\mathbf{F} = q\mathbf{v}\times\mathbf{B} - m\nu_c\mathbf{v}\,. \tag{1.1}$$

The term $\nu_c\mathbf{v}$ may be regarded as a fictitious deceleration term describing the slowing down of an 'average' particle due to collisions with a background gas [3]. In an actual

collision, the particle will recoil at some new angle and velocity which depends on the details of the process. It is impractical to model such processes for great numbers of particles and collisions, and it is unnecessary, as the average effect is a net slowing down of the energetic particle in a lower energy bath of 'cold' gas or plasma. In a thermonuclear fusion reaction in MIF, the particle will transfer kinetic energy via scattering collisions to thermal energy in the much colder background plasma in the magnetized target. The desired effect is for the heating rate by alpha deposition to exceed thermal transport and radiation losses, thereby achieving thermonuclear fusion ignition in the target. While deposition power is important for most fusion confinement approaches, our efforts are concentrated on the application for MIF. Three of the dominant fusion confinement concepts are presented below to justify our choice of MIF.

1.2. Nuclear Fusion

Nuclear fusion is the exothermic reaction in which two or more lighter nuclei merge together to form a heavy nucleus. The process of nuclear fusion requires high particle energies to overcome the mutual Coulomb repulsion of the atomic nuclei. Many approaches to fusion achieve this by raising the fuel to hundreds of millions of degrees [4], and these are collectively called thermonuclear fusion.

Fusion energy is of great interest, since the byproducts need not be radioactive, and there is an abundance of fuel in the world's oceans to supply sufficient world energy demands for centuries. One of the major hindrances in thermonuclear fusion is the challenge of confinement of the plasma due to the high temperatures, and consequently, fusion concepts are often categorized by their confinement scheme. Among the leading

approaches are Inertial Confinement Fusion (ICF), Magnetic Confinement Fusion (MCF), and Magnetoinertial Fusion (MIF).

1.2.1. Inertial Confinement Fusion

In inertial confinement fusion, a fuel pellet is compressed by the rapid ablation of the outer shell, which is called the ablator, Figure 1.1. The ablator encloses the main fuel as frozen or liquid deuterium-tritium (DT). As shown in Figure 1.1, the spherical shell is targeted with very high powered laser beams that ablate the outer layer of the target Figure 1.1 (a).

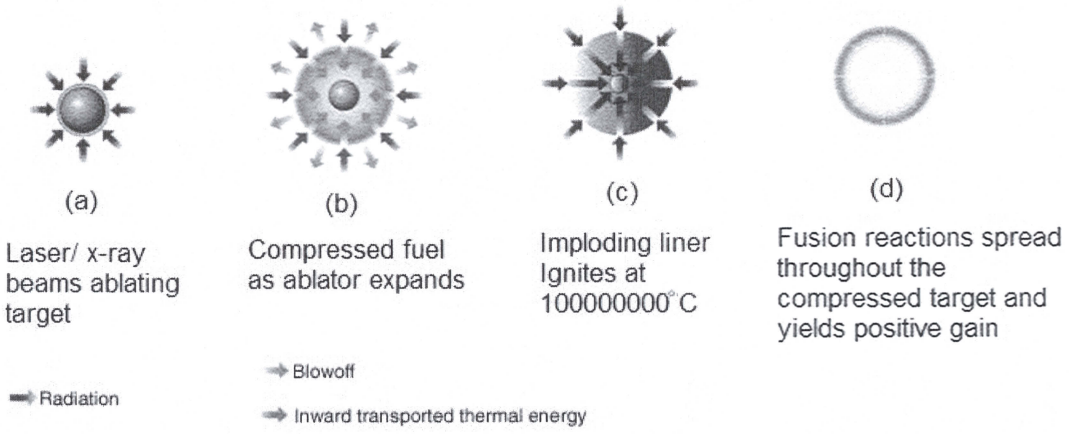

Figure 1.1 Inertial confinement fusion

The driver delivers its energy to the target, heating and expanding the ablator. Due to momentum conservation, the inner shell gets compressed (Figure 1.1 (b)). The Compressional work further increases the temperature at the center of the target, resulting

into self sustaining burn of the fuel, Figure 1.1 (c, d) [5]. ICF generally needs densities as high as 10^{29} m^{-3} and temperatures of 10keV. No magnetic field is used in this approach.

1.2.2. Magnetic Confinement Fusion

In magnetic confinement fusion, a ~10^8 K plasma is confined by high magnetic fields of more than 5T. Electron and ion densities range from $10^{20}m^{-3}$ to $10^{22}m^{-3}$. The ratio (β) of plasma pressure to the pressure of the external magnetic field which confines the plasma is an important quantity in the physics of magnetic confinement fusion [6]

$$\beta = \frac{p}{(B^2 / 2\mu_0)}, \tag{1.2}$$

where the plasma pressure **p** in is given by

$$p = nkT, \tag{1.3}$$

where n is number density of the plasma, k is Boltzmann's constant and T is the temperature of plasma. In the low β (~0.01) regime, the poloidal magnetic field suppresses the drift of the charged particles, thereby achieving confinement of the fusion plasma [7]. A toroidal field, on the other hand, improves thermal insulation and enhances stability [8].

1.3. Magneto-Inertial Fusion

Magneto-inertial fusion (MIF) seeks to combine the favorable attributes of the low reacting volume of ICF by using a high density plasma and the suppression of electron thermal conduction in MCF by using a magnetic field [9]. MIF works in an intermediate regime between ICF and MCF, Figure 1.2. Since fusion reactivity is directly proportional to the square of the plasma density [10] and MIF plasmas are roughly 10^6 to

10^8 denser than MCF, MIF reactivity is 10^{12} to 10^{16} times more than that of MCF. The magnetic field in MIF reduces the heat losses by suppressing the cross field electron thermal losses [11] which reduces the power requirement for the drivers needed for target compression [12]. The system size is thus reduced compared with ICF since mass is scaled with the power requirements of the drivers.

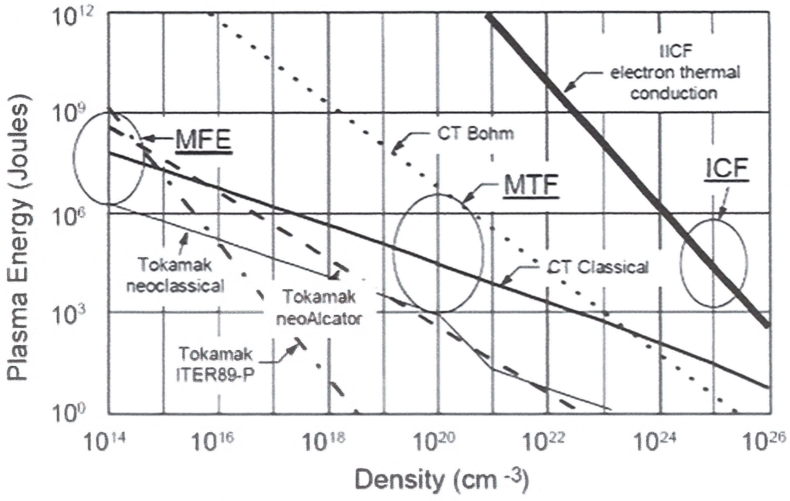

Figure 1.2 Plasma energy required vs plasma density for different configurations [13]

In MIF, the fusion fuel is contained in the magnetized target. The target is typically a compact toroid, which is a simply connected plasma with closed field lines. These are further classified into spheromaks or Field Reverse Configurations (FRC). FRC's are different from spheromaks due to the absence of a toroidal field.

There are two major embodiments for MIF distinguished by the liner material, geometry, and compression scheme. Solid liner MIF utilizes a cylindrical metallic shell which implodes on a magnetized target. The implosion is caused by driving a large

current (~12 MA) through the shell, which causes a self-compression due to the Lorentz force proportional to **jxB**. A plasma liner driven MIF uses plasma guns or other means to form a spherically imploding plasma shell which compresses a magnetized target. Our alpha deposition model, and the results therein, are independent of the liner approach. However, for completeness, we discuss these in some detail below.

1.3.1. Solid Liner MIF

In solid liner driven MIF, an imploding aluminum shell compresses the magnetized target [14]. An FRC is translated inside a cylindrical aluminum liner as shown in Figure 1.3. The high energy (up to 5 MJ) capacitor banks discharge the large amount of current (~12 MA) into the aluminum liner which radially crushes the target and the liner with an implosion velocity of around 20 km/s [15]. A compression ratio (ratio of starting radius of liner to final implosion radius) of 10 has been obtained in recent experiments [11].

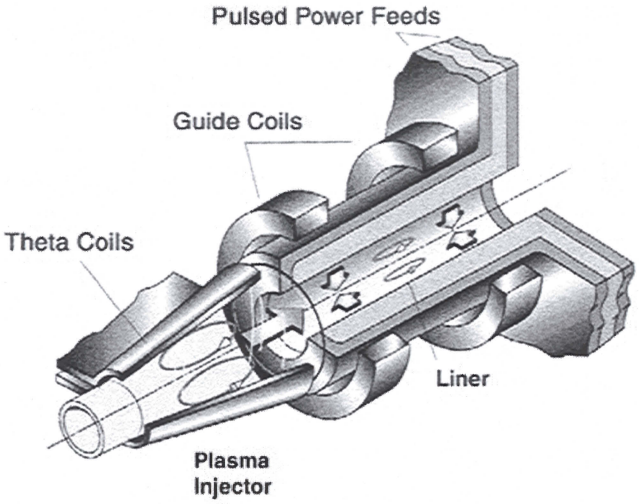

Figure 1.3 Solid liner MIF concept using a field reversed configuration plasma [16]

1.3.2. Plasma Liner Magnetoinertial Fusion

Plasma liner driven MIF has its roots in impact fusion, which is an approach to ICF. Lack of suitable driver (a 0.1gm of solid projectile at 200km/s) needed to achieve necessary ignition conditions was one of the major issues [17]. Thio [12] proposed the use of a large number (~60) of pulsed plasma guns, which collectively provide the requisite velocity and total mass needed. This thinking, combined with the emerging solid liner MIF concept, led to the plasma liner approach for MIF.

The basic approach consists of the plasma guns placed on an evenly distributed spherical or cylindrical surface. Each plasma gun shoots simultaneously at the center. The jets merge at a stand-off distance from the center proportional to the jet diameter and

number of jets. Separately, the magnetized target is formed and translated into the spherical chamber. Figure 1.4 shows a cylindrical array of plasma guns which forms the plasma shell [12], compressing the target.

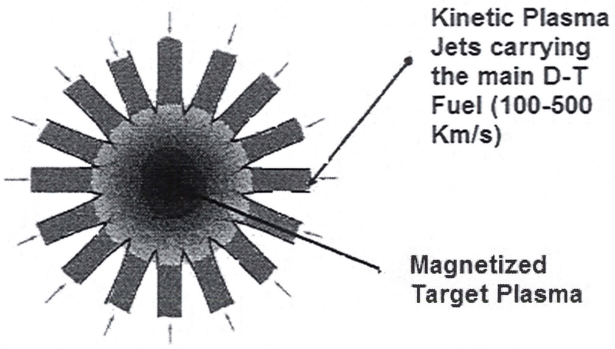

Figure 1.4 Cylindrical array of plasma guns to form a plasma liner [12]

1.4. Ignition

In either embodiment of MIF, the goal is for the target/liner system to reach ignition. The term 'ignition' has different meanings in ICF and MCF plasmas. In MCF, ignition occurs as thermonuclear energy deposited in one energy confinement time equals the energy supplied to the system to reach thermonuclear burn temperatures. In ICF, ignition occurs when alpha particle deposition and thermonuclear energy production in the core of the target achieves the temperature required for self sustaining burn that spreads throughout the target [5]. In this thesis, we define ignition as a state of the system in which the fusion heating power exceeds the thermal losses.

The fusion heating power is due to a translation-translation energy transfer from energetic fusion products to the cold background plasma via scattering collisions. A

neutron and a charged particle (proton, alpha particle) are the products of a fusion reaction between deuterium and tritium nuclei, in accordance with

$$ {}_{1}^{2}\mathrm{D} + {}_{1}^{3}\mathrm{T} \rightarrow {}_{2}^{4}\mathrm{He}(3.52\mathrm{MeV}) + \mathrm{n}^{0}(14.06\mathrm{MeV}), \tag{1.4} $$

Neutrons escape the plasma very easily since they have very high birth velocity and are not affected by magnetic or electric field. Some charged particles (alpha-particles), however, get trapped as a result of collisions and deflection due to the electric or magnetic fields [18].

Since neutrons cannot be trapped, the deposition of alpha particles plays a crucial role in providing heating power to the target during thermonuclear burn. Significant deposition can occur only when either the collision mean free path and/or the Larmor radius is less than the target radius. Solid densities are necessary for the former condition, thus requiring MIF targets to have a sufficiently high magnetic field. The deposition heating is nonlocal, and exact analytical treatment is not possible for general compact toroid topologies. Thus, numerical modeling of the alpha deposition is needed for determining the ignition condition. We are, therefore, investigating the alpha particle deposition in FRC's to help determine the ignition conditions for MIF applications.

1.5. Roadmap to Thesis

The alpha particle energy deposition model for FRC is discussed in Chapter 2. A brief background and the physics of the FRC are also presented in the same chapter. In Chapter 3, the plots of alpha energy deposition in the FRC as a function of different parameters such as magnetic field, density and elongation are analyzed. We developed a curve fitting model to the results to calculate some ignition conditions using Lindl-

Widner diagrams. The Lindl-Widner model and results are given in Chapter 4. Chapter 5 provides a summary of the work done and gives concluding remarks.

CHAPTER 2

ALPHA DEPOSITION

We have developed an alpha particle deposition model for a field reversed configuration (FRC) plasma in an effort to assess its potential benefits for magnetoinertial fusion (MIF). Here we describe basic particle-level physics of deposition and discuss relevant research in alpha deposition in magnetized targets, the magnetic field topology of FRC's, and the numerical model developed and utilized.

2.1. Background

Alpha deposition is a source of non-local energy transport, causing target heating due to intermolecular collisions of fusion alpha particles with ions and electrons in the target. The alpha particles (^{4}He) are the high energy (3.5 MeV) charged helium ions produced in a DT (deuterium-tritium) fusion reaction. During a collision, an alpha particle transfers a fraction of its energy to the much colder ions and electrons, thereby heating the target. The physical process can increase the burn time of the target and relax the heating power required of the imploding liner. Self heating by alpha particle deposition is necessary for ignition of MIF targets. The alpha heating power can be

significant in MIF targets for fields in which the Larmor radius $r_{L,\alpha}$ is less than the target radius, even though the collisional mean free path is many times the target scale length, which is ~1 to 10 cm. In principle, it would be possible to create target conditions to effectively capture all of the alpha particle energy as will be shown, but that may require unnecessarily high target fuel density and/or magnetic field strength.

Kirkpatrick [19] used an analytical approach to calculate the deposition of alpha particle energy in a target. Kirkpatrick's model used the collisions of alpha particles with ions and electrons to slow the alpha particles and absorb some of the alpha particle energy [20].

Basko and Kemp developed a model to calculate the fraction of the alpha particle energy deposited in a cylindrical target with an axial magnetic field [3]. The model simulated single alpha particle trajectories in which the birth velocity vector and position were the independent variables. The average energy per particle deposited before leaving the target was determined in order to determine the fraction of deposited energy. Trajectories were determined by integrating the classic equations of motion for a charged particle subject to a magnetic field and an average collision frequency as given in Equation. (1.1). The motion represented an average 'swarm' of the particle, in that the collision term slows the particle down and is taken as a statistical average motion per particle due to a scattering collision [21]. Using the numerical results, they were able to collapse the deposition to a function of two variables, $\bar{R}$ and b, where $\bar{R}$ is the ratio of the target radius to the Coulomb range of the alpha particle and b is the ratio of the target radius to the alpha Larmor radius $r_{L\alpha}$ at the birth. They determined an approximate

expression for f_α, the deposited alpha energy fraction to within 3% of the numerical values given as

$$f_\alpha = \frac{x_\alpha + x_\alpha^2}{1 + 13x_\alpha/9 + x_\alpha^2}, \tag{2.1}$$

where

$$x_\alpha = \frac{8}{3}\left(\bar{R} + \frac{b^2}{\sqrt{9b^2 + 1000}}\right). \tag{2.2}$$

Basko and Kemp limited their study to cylindrical targets with purely axial magnetic fields.

Thompson extended the work of Basko and Kemp to spherical closed field line topologies [11]. The field topology was purely uniform in the azimuthal direction, which led to a second order drift which caused particles to 'leak' along the poles.

In MIF, the magnetized target field topology will probably be a compact toroid [22], in which the field lines are closed. Such topologies are advantageous because they are simply connected and do not have end losses. However, compact toroids are difficult to treat analytically. We have expanded on the numerical work of Basko and Kemp and Thompson and have applied it to FRC targets. The FRC field topology and relevant physics are discussed in the following section.

2.2. Field Reversed Configuration (FRC) Topology

Compact toroids (CT's) [2] [8] are high β plasmas noted for compact geometry. They can be classified with the s-parameter given by [2]

$$s = \frac{r_{\text{torus. minor}}}{r_{\text{Larmor}}}, \tag{2.3}$$

where $s \gg 1$ means MHD-like. They can also be characterized with the ratio of poloidal (B) to toroidal (B_θ) internal magnetic fields. Table 2.1 summarizes the different types.

Table 2.1 Types of compact toroids. 'B' refers to poloidal field and 'B_θ'

	s>1	s<1
$B \gg B_\theta$	FRC	
$B \gg B_\theta$ or $B \sim B_\theta$	Field Reversed Mirror (FRM)	Astron
$B \sim B_\theta$	Spheromak	

The Field Reversed Configuration (FRC), as identified in the table above, is typically characterized as an elongated prolate (cigar-shaped) compact toroid with no toroidal field [2], Figure 2.1. There are two regions: a closed field line torus enveloped by an open field line sheath. The boundary separating these two regions is called the separatrix, Figure 2.1, and the separatrix radius r_s is measured from the axis of symmetry to this boundary. A cutaway of a theta pinch coil is shown in this figure, since a common way to form these plasmas is to discharge an underdamped capacitor bank through a theta pinch. Theta pinch currents are typically of the order of 100 kA to 1 MA with a ringing frequency of 1 MHz.

From the perspective of this work, we are primarily interested in approximating the internal structure of the magnetic field and thermodynamic properties in order to provide a reference for our alpha deposition model. While studies in FRC physics are rich from microscopic to macroscopic scales, it is beyond the scope of this work to

provide a comprehensive treatise of that field of research. Nevertheless, for completeness, we provide a brief summary of past FRC research to direct the interested reader.

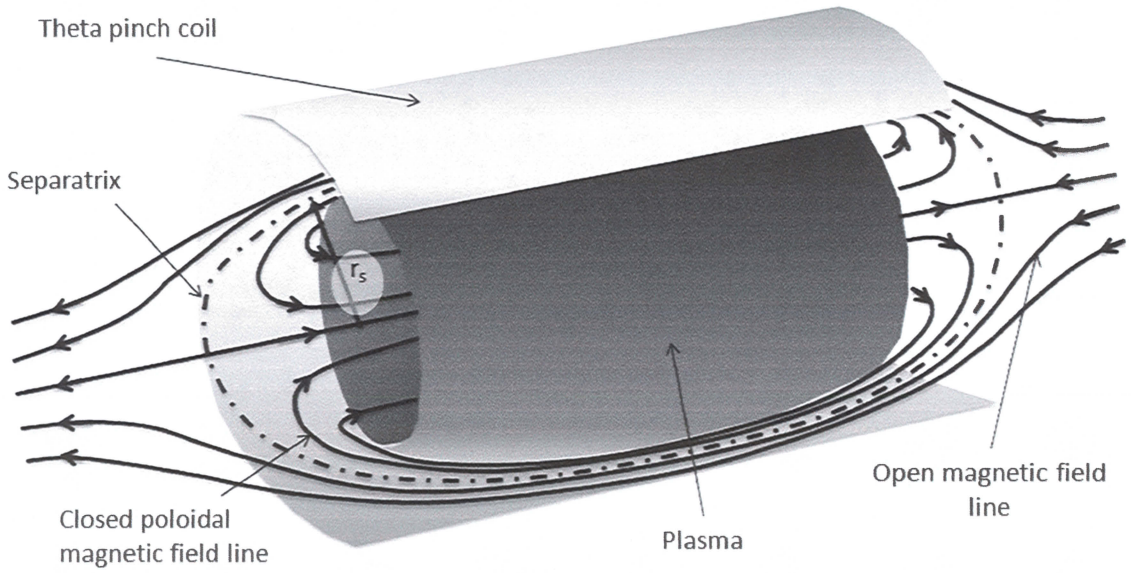

Figure 2.1 Field reversed configuration schematic. The theta pinch coil is cut away for illustrative purposes, but typically would consist of a single turn coil surrounding the plasma.

Ostensibly, the FRC was an accidental discovery as a result of early theta pinch research in 1958. The first FRC's were formed as shown with reverse bias field and theta pinch, but can be formed by rotating magnetic fields, coaxial geometries, and theta pinches [2]. Since then, some theta pinch experiments have been devoted to FRC research, and have emphasized various global issues such as formation [23], confinement [2], heating [23], and rotation [14]. More recent experiments have probed deeper into internal FRC physics involving topics such as the n=2 instability and

transport [24]. The recent research at various facilities like the University of Washington, Osaka University, Nihon University, and Tokyo University have contributed to an improved parameter range of FRC operation given by [25],

Density	$0.5-50\times10^{14}\,\mathrm{cm}^{-3}$
Ion temperature	$50-2000\mathrm{eV}$
Electron temperature	$50-500\mathrm{eV}$
Average β	$0.9-0.95$

In order to provide a model of the FRC for our alpha deposition model, we consider an elongated FRC inside a cylindrical flux conserver with sharp boundaries, such as those which have been studied by Wright et al. [26] and Kadish [27]. In these models, a force-free field reversed configuration is assumed,

$$\nabla\times\vec{B}=\alpha\vec{B}, \tag{2.4}$$

with density set to offset the magnetic field in accordance with the pressure balance, assuming a uniform temperature. In the equations below, we appeal to Figure 2.2, which shows a 2D slice through an axisymmetric FRC. The contour lines are in the r-z plane and are tangent to the magnetic field. The current is azimuthal and orthogonal to the page. The contours are colored against the relative value of the density, which varies in r and z. We assume no toroidal component of the field ($B_\theta=0$), with the radial and axial fields given by

$$B_r=-B_0\frac{k}{\lambda}J_1(\lambda r)\cos(k(z-z_0)) \tag{2.5}$$

$$B_z=B_0J_0(\lambda r)\sin(k(z-z_0)). \tag{2.6}$$

r and z are radial and axial positions respectively, $k = \pi/(2z_0)$, and $\lambda = 3.8317/r_s$. Note that k and λ cause the field to be parallel to the conducting surface when $r=r_s$ or $z=\pm z_0$. The density is given by

$$\rho = \rho_0(1+\frac{k^2}{\lambda^2})J_1(\lambda r)(\sin(k(z-z_0)))^2, \tag{2.7}$$

where $\rho_0 = n\times 2.5\times 1.6605\times 10^{-27}$ is proportional to the mass density amplitude in kg/m^3 and n is number density of plasma in particles/m^3. This configuration allows us to study the effects of elongation, which may be important for cylindrical compression schemes. As an extension, we may consider a spherical closed field topology such as is given by the Solov'ev model [30, 31] in future work.

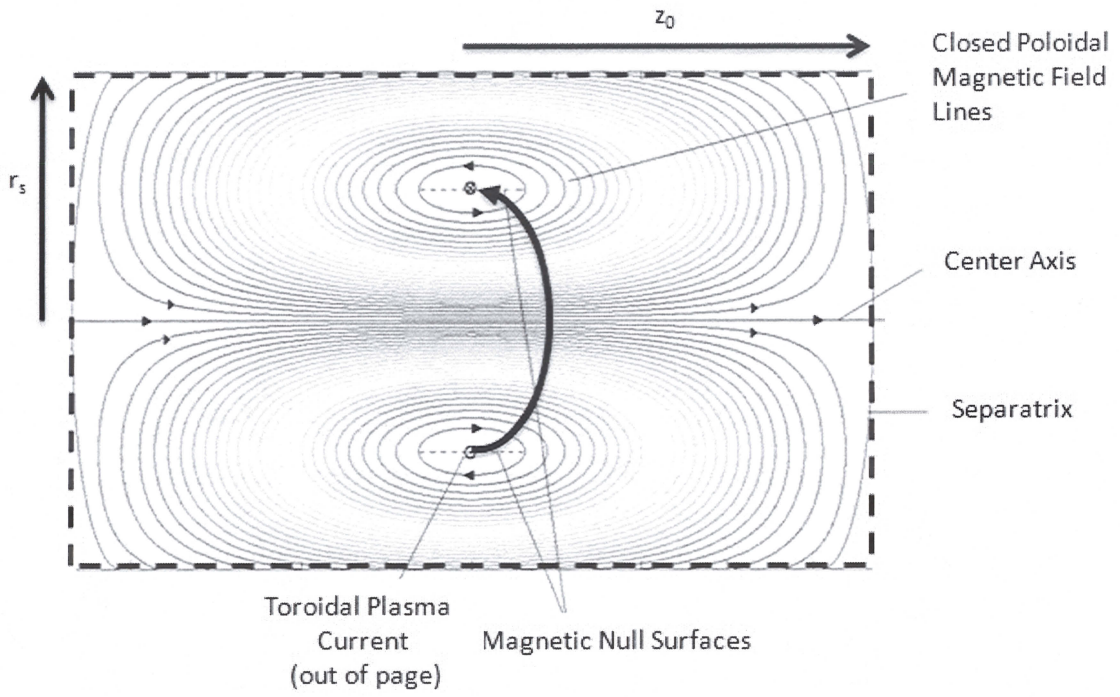

Figure 2.2 2D slice through an axisymmetric FRC with magnetic field topology (contours) and density profile (contour colors) shown. The dashed box represents the flux conserving cylindrical boundary.

The system is cylindrically symmetric about the center axis, Figure 2.2. The surface (dashed line) enclosing all closed field lines is the separatrix. The cylindrical null is formed in the FRC where the magnetic field goes to zero. The magnetic fields in the center of the FRC, where field lines are parallel to the center axis, do not vary significantly in the axial direction. However, the magnetic field toward the end where it starts bending is a strong function of the axial direction. The magnetic field along the

center axis reverses its direction inside the FRC [23]. These field lines encircling the magnetic null axis are called lines of poloidal flux [8].

2.3. Qualitative Description of Alpha Particle Motion in an FRC Target

The alpha particle trajectory depends on the magnitude of the density and the strength of the magnetic fields determined with Equations (2.5), (2.6), and (2.7). In the low density, low magnetic field case where $r_{L\alpha} \gg r_s$, the alpha particle trajectory is essentially a straight line in the direction of the birth velocity vector, with little deceleration. With a significant increase in density so that many collision mean free paths reside in the target, the trajectory will still remain a straight line, but the alpha particle will experience significant deceleration in the target. When the magnetic field is sufficiently high such that $r_{L\alpha} \ll r_s$ and the particle is not born near the surface, the alpha particle will remain trapped and experiences various drifts such as $\nabla\vec{B}$ drift, $\vec{E}\times\vec{B}$ drift, Lorentz forces, etc. The interaction of the particles with these forces decides the trajectory of particle in the target. For illustration purposes, we discuss grad B drift in more detail.

Figure 2.3 shows the grad B drift for alpha particles moving near to the null magnetic surface in the FRC. Particles traveling above or below the null surface will observe a gradient in magnetic field ∇B, directing away from the null surface. The Magnetic field B below the null surface is in the +z direction and the field above is directed in the -z direction. The gradient drift experienced by an alpha particle in both locations is given by [30]

$$v_{grad} = \pm \frac{v_\perp^2}{2\omega_c} \frac{B \times \nabla B}{B^2}, \tag{2.8}$$

where ω_c is gyro frequency of a particle and $v_\perp$ is the azimuthal velocity,

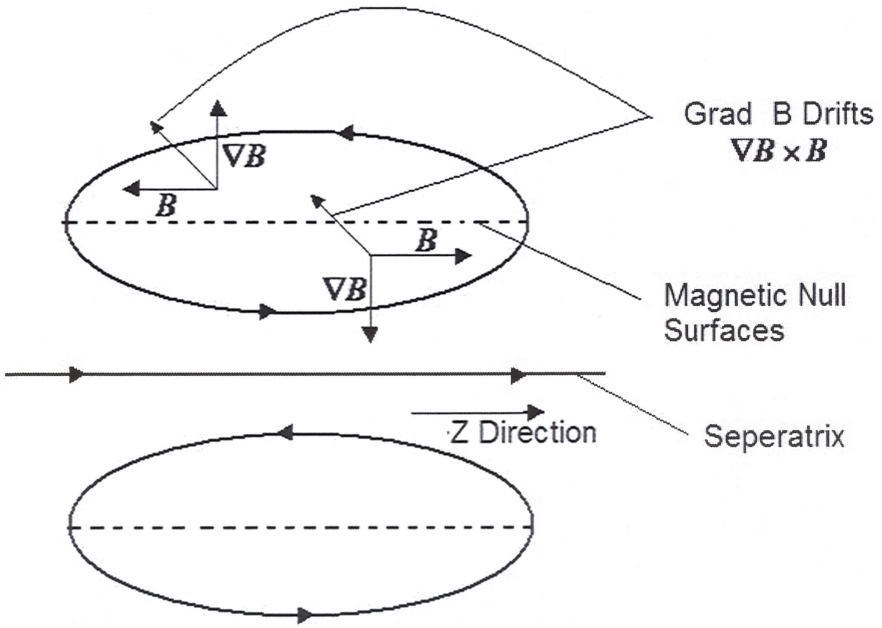

Figure 2.3 Grad B drifts in FRC's.

2.4. Alpha Deposition Model

Our deposition model is based on integrating a set of differential equations to track individual particle motion. A particle moving in a steady magnetic field will experience an acceleration perpendicular to both the velocity and magnetic field (See [33], for example) direction according to

$$\dot{\vec{v}} = \frac{Zq}{m}(\vec{v} \times \vec{B}) - \nu \vec{v}, \tag{2.9}$$

where $\vec{v}$ is velocity vector, $\vec{B}$ is the magnetic field, Z is the charge number of the particle (2 for alpha particle), q is the elementary charge, and m is mass. The collision frequency is determined with

$$\nu = \frac{v_{\alpha 0}}{l_\alpha}, \tag{2.10}$$

where l_α is the Coulomb interaction length given by

$$l_\alpha = \frac{3}{4\sqrt{2\pi}} \frac{m_\alpha v_{\alpha 0} T^{\frac{3}{2}}}{Z_\alpha^2 q^4 n m_e^{\frac{1}{2}} L_\alpha}, \tag{2.11}$$

In this equation m_α is the mass of an alpha particle, $v_{\alpha 0}$ is the birth velocity of the alpha particle, T is the temperature of the alpha particle in keV, n is the particle density, m_e is the electron mass, and L_α is the Coulomb logarithm. The Coulomb logarithm is estimated at $L_\alpha = 7$ [3].

The Cartesian equations of motion assuming a steady magnetic field are [33]

$$\begin{aligned} \dot{v}_x &= \omega_z v_y - \omega_y v_z - \nu v_x \\ \dot{v}_y &= \omega_x v_z - \omega_z v_x - \nu v_y \\ \dot{v}_z &= \omega_y v_x - \omega_x v_y - \nu v_z \end{aligned}, \tag{2.12}$$

where

$$\omega_{x,y,z} = \frac{ZqB_{x,y,z}}{m_\alpha} \tag{2.13}$$

are the gyrofrequencies for the x, y, z components of the plasma. By integrating the set of equations in (2.12), the position of the particle can be determined as a function of time.

For illustrative purposes, a sample trajectory is given in Figure 2.4. The particle is born at z=2, x=3.606, y=3.606. The magnetic field strength and density vary, but the

volumetric average is 3.2 T and 1.644×10^{24} #/m^3, respectively. In this case, the particle is trapped and bounces between two points where the magnetic field is higher. The kinetic energy parallel to the field is highest at the top point of the arc, and zero at the ends of the arc. In a collisionless case, the periodicity observed in this trajectory could be described using the adiabatic invariant μ and conservation of energy. There is a higher order drift caused by the grad B and curvature drift which causes precession of the bounce orbit, similar to that of an electron bouncing between the north and south magnetic poles of the earth.

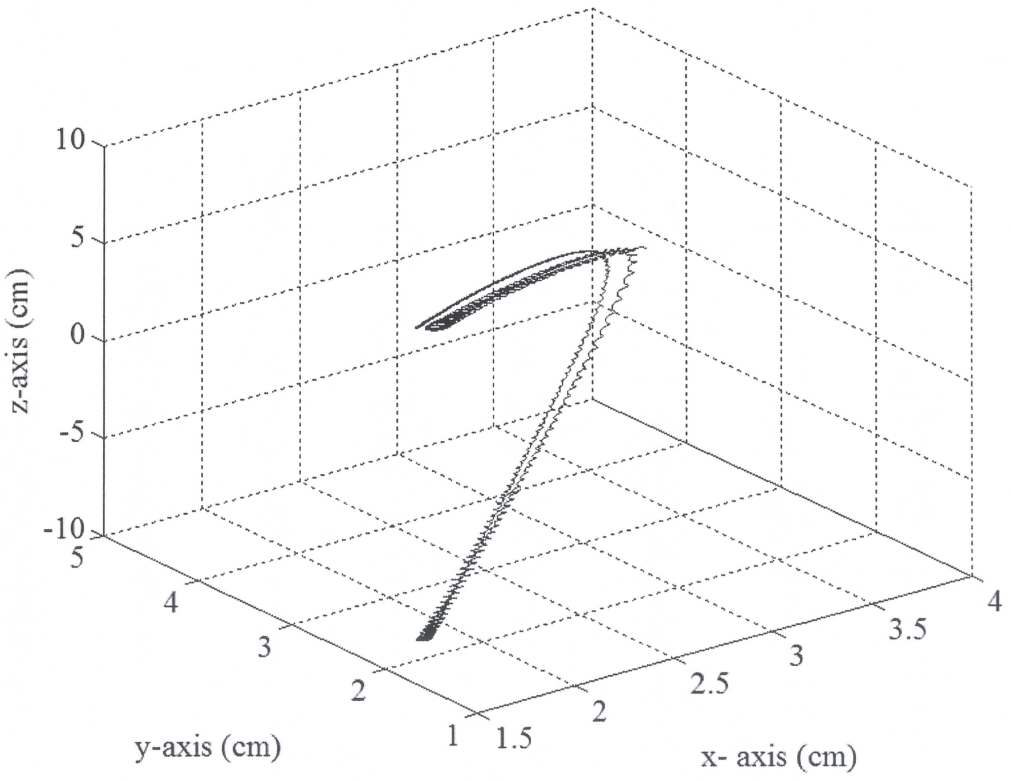

Figure 2.4 Sample trajectory of an alpha particle in an FRC.

Not all particles are trapped such as is shown in Figure 2.4. If a particle crosses the target surface, we assume that the particle does not return. Several factors can lead to particles leaving the target. First, as was discussed in the previous section, if the magnetic field and density are low, the trajectories are essentially straight lines. For sufficiently high magnetic field, the particles may be trapped. However, in certain topologies, 2^{nd} order particle drifts may cause particle leakage. In FRC's, the second order drifts all lead to internal motion that does not result in particle loss at the surface. These particle drifts are mainly due to curvature and gradients in the magnetic field topology. The gradient drifts in FRC's were discussed previously in Section 2.3 (Figure 2.3).

Scattering collisions will cause the particle to 'walk' randomly to other field lines and consequently, may lead to particle loss. However, because of the disparity in velocity between the fast alpha particles and the background plasma particles, which are effectively stationary, the scattering angle is typically very small. On average, the net effect will be deceleration, so the random walk effect is not included in the model discussed in the following section. This assumption is consistent with the work of Basko and Kemp [3], who state that the random walk effect or Bohm's diffusion would not affect the results since in MIF, the plasma to cyclotron frequency ratio is high. Further, the $\vec{E} \times \vec{B}$ drift cannot establish itself due to fluctuations in E [32].

With the equations above, our model is run on a 4D grid (2 in velocity space and 2 is the r-z plane). The integration for a given particle is stopped when either the particle

reaches the radius of the target or loses 99% of its energy. Energy deposition is determined then by calculation of the average energy deposited per particle.

2.4.1. Energy Deposition

To find the average energy deposition, we made the assumption that the birth velocity vector and position were isotropic within the target. We then established a four-dimensional grid in which θ, Φ, r, and z were the coordinates, with the spatial coordinates shown in Figure 2.5. The angles describe the birth velocity vector, with θ varying from 0 to π radians, while Φ varied from 0 to 2π. The physical coordinates r and z represented evenly spaced points within the limits of the target surface. The particle is placed with starting energy of 3.5 MeV. For each set of 4D coordinates, the system of equations given in Equations (2.12) is integrated using Matlab with ODE45, a 4^{th} order Runge Kutta numerical integration scheme [35].

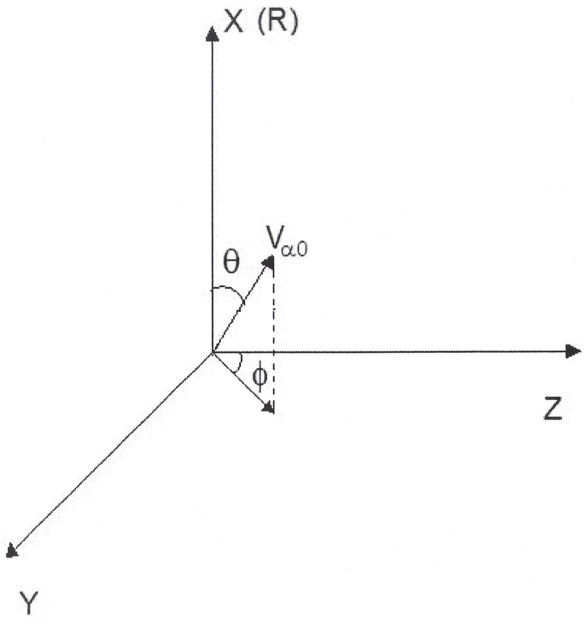

Figure 2.5 Coordinate system for initial position and born-on velocity vector for an alpha particle.

To calculate the deposited energy per particle, we use the final kinetic energy of the particle as it leaves the target,

$$KE = \frac{1}{2} m v_{\alpha}^{2} . \tag{2.14}$$

The fractional deposited energy the particle leaves in the system is then

$$f_{\alpha} = 1 - \frac{v_{\alpha}^{2}}{v_{\alpha 0}^{2}} . \tag{2.15}$$

The deposited energy from each particle is stored and then averaged over the solid angle of the cylindrical geometry with

$$f_{\alpha_{average}} = \frac{2}{R^2}\int_0^R rdr \frac{1}{l}\int_0^z dz \frac{1}{4\pi}\int_0^{\pi} \sin\theta d\theta \int_0^{2\pi} f_\alpha d\phi . \tag{2.16}$$

Integrations in Equation. (2.16) are approximated using the trapezoidal rule.

The range for these parameters is given below in Table 2.2. We chose these values to be consistent with the typical MIF parameter space [36]. The variables 'b' and '$\bar{R}$' are dimensionless parameters given by,

$$b = \frac{R}{r_{\alpha L}} \tag{2.17}$$

and

$$\bar{R} = \frac{R}{l_\alpha}, \tag{2.18}$$

where R is the target radius and $r_{\alpha L}$ is the Larmor radius. We vary b from 10^{-6} to 10^{2} which gives a magnetic field density range of 2.69×10^{-3} to 2.69×10^{3} Tesla. Similarly, $\bar{R}$ is varied from 10^{-3} to 10^{3} which results in a number density range from 1.64×10^{22} to 1.64×10^{30} #/m^3. Elongation is the length to radius ratio of the FRC. We chose these values to assess the difference in deposition between 'short' and 'long' FRC's. We chose an absolute scale length of 10 cm, which is typical of FRC targets.

Table 2.2: Parameter range for the alpha deposition model.

Variable	**Range**
b	10^{-6} to 10^{2}
$\bar{R}$	10^{-3} to 10^{3}
Elongation (Z/R)	0.5,1,2,5
Density	1.64×10^{22} to 1.64×10^{30} #/m^3
Magnetic field (B)	2.69×10^{-3} to 2.69×10^{3} Tesla
ϕ	0 to π
Θ	0 to 2π

CHAPTER 3

RESULTS AND ANALYSIS

With the model and parameter range given in Chapter 2, we calculated the fractional alpha deposition as a function of four independent variables which are collapsed to a two-dimensional space. Code verification tests were performed to provide confidence in the numerical output. These included resolution convergence tests where the computational 'grid' consists of subdivisions in both physical and velocity space. Qualitative tests were performed to make sure that certain asymptotic behaviors were observed. With confidence in the output, the alpha deposition curves are presented. Curve fits to the alpha deposition results are given, which are then utilized in the proceeding chapter in the construction of Lindl-Widner diagrams.

3.1. Code Verification

In order to provide confidence in our alpha deposition results, we ran a series of tests to provide an estimate of both the error and rate of convergence. The goals included providing an estimate of the error in our code to insure that our results were conservative, meaning that the deposition predicted would be less than or equal to the actual value for a given set of conditions.

The first test was to run the code to model a geometry and magnetic field topology with a known solution for the deposition, which helps to quantify the error and convergence rate. Since the solution is only good for the low density, low magnetic field limit, we ran subsequent tests to assure that the deposition goes to 1 in the high density/high magnetic field limits. Finally, for the FRC topology in which the solution is not known, we can only put bounds on the deposition in various limits and estimate the self-convergence rate (explained below).

3.1.1. Infinitely Long Cylinder, Purely Axial Field Test Case

The test case was a solution to an infinitely long cylindrical target with axial, uniform magnetic field as was examined by Basko and Kemp [3]. For $\bar{R} << 1$, the deposition is $f_\alpha = \frac{8}{3}\bar{R}$. To estimate the convergence, we calculated the relative error with

$$\epsilon = \frac{f_{\alpha,N} - f_{exact}}{f_{exact}}, \tag{3.1}$$

where $f_{\alpha,N}$ is the fractional alpha deposition for n grid points. In general, the 'grid' is the total number of points in the velocity and physical space, i.e., the product of the number of subdivisions in θ, Φ, r, and z. For the infinite cylinder, the z coordinate is eliminated, reducing this to a three-dimensional problem. Further, we found that the error was insensitive to θ as long as we varied the angle in increments no smaller than π/2, so that only four θ angles were needed, thus reducing the grid size to $n=4\times n_r \times n_\Phi$.

In order to estimate the rate of convergence, we can use the following procedure. A sequence will converge to some value ξ with order p if

$$|x_n - \xi| < Cn^{-p}, \tag{3.2}$$

where C is a constant and n is the number of grid points. One way to estimate the coefficients is to plot the function and the data in log-log space. The slope of the line is p, and C shifts the curve vertically. To satisfy the criterion above, the slope of the curve must be greater than or equal to that of the data, and the ordinate of the curve must be equal to or greater than any of the data at a given value of n. Following this procedure, we found the rate of convergence to be of the order $n^{1/2}$, with the error and convergence curve shown below. We found that the deposition was *underestimated* by ~50%, 18%, and 7%, respectively, for $n=10^2$, 10^3, and 5×10^3, respectively. It should be noted that the wall clock computational time was roughly linear with n.

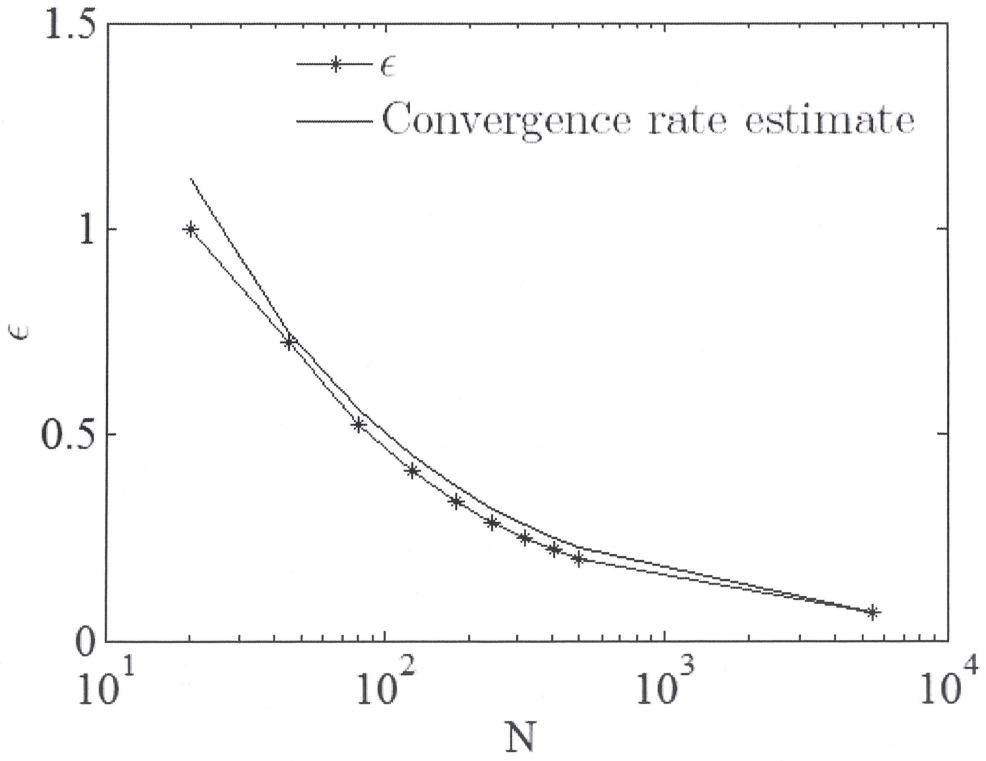

Figure 3.1 Error between alpha deposition code and exact results for infinitely long cylinder with uniform axial magnetic field. Convergence rate curve is shown for comparison.

3.1.2. Asymptotic Tests

We investigated asymptotic behavior for both infinitely long cylindrical targets with uniform magnetic field and truncated cylinders with FRC magnetic field topology. In either case, as $\bar{R}$ or $b \to \infty$, $f_\alpha \to 1$. This behavior was observed for both the uniform,

infinitely long cylinders and for the FRC targets. Additionally, for $b \ll 1$ and $\bar{R} \ll 1$, since $f_\alpha = \frac{8}{3}\bar{R}$ for the infinitely long cylinder, a truncated cylinder with the same $\bar{R}$ and b values should have a lower value for f_α due to the particle loss at the ends. Again, this was observed in all results produced by our code.

3.1.3. Self Convergence in the High *b* Limit

Since there is no known general solution for the alpha deposition in an FRC topology, we verified that certain asymptotic behaviors were observed as discussed above. Additionally, we estimated the self-convergence rate for $b = 100$, for which we estimate that the deposition should be ~0.95 to 0.99. A self-convergence test is typically performed for grid resolution studies in which an answer is not known. The criterion becomes

$$\left|x_n - x_{n+1}\right| < Cn^{-p}, \tag{3.3}$$

where the difference is taken between results produced by the code at subsequently finer grid resolutions. This technique requires that the code converges as $n \to \infty$. The maximum error, and consequently, the lowest convergence rate, could be found if we assumed that the actual value of the deposition was 1.0 so that

$$\left|f_{\alpha,n} - 1\right| < Cn^{-p}. \tag{3.4}$$

We note that the error is also equal to $\left|f_{\alpha,n} - 1\right|$. The results are shown below. We found that the worst possible convergence rate was $\sim n^{0.07}$.

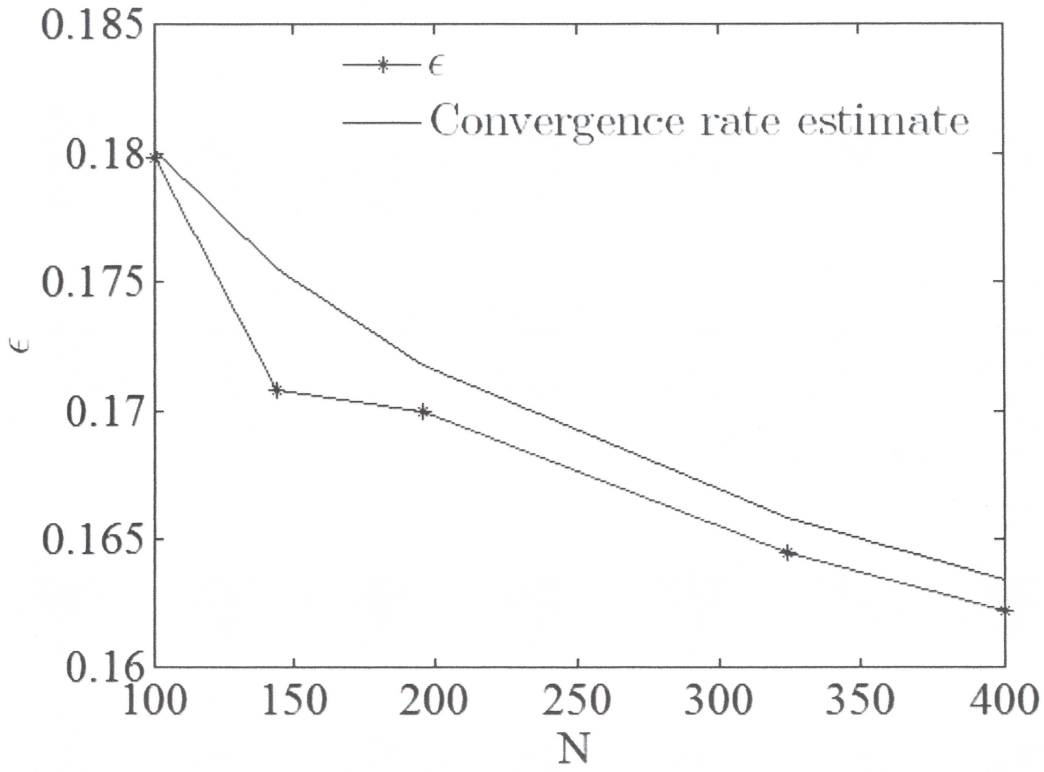

Figure 3.2 Maximum possible error between alpha deposition code and actual deposition in an FRC target. Convergence rate curve is shown for comparison.

3.1.4. Assessment

We observed the code always produced the correct qualitative trends. Specifically, in the high density, magnetic field limits, the deposition goes to 1.0. In the low density limit, the deposition becomes independent of magnetic field and is somewhat less for the truncated cylinders than with the infinitely long cylinders. Further, for the grid resolution we used for the results we present below, the code produces deposition values consistently 10 to 20% below those of either known solutions or maximum

possible solutions. This satisfies our criteria that the numerical output reflects the qualitative trends and provides a conservative estimate of the deposition.

3.2. Alpha Deposition Modeling

With confidence in our numerical output, we present the alpha deposition results in the following section.

3.2.1. Numerical Results

As described in Chapter 2, we plotted alpha deposition as a function $\overline{R}$ and b. This was performed at fixed values of FRC elongation. These data are given in Figure 3.3 – Figure 3.6 for elongations of 0.5, 1, 2, and 5, respectively. Each chart shows curves of f_α vs. b at constant $\overline{R}$. We first observe that there is very little difference in the results as a function of elongation. For the remaining discussion, we focus just on Figure 3.3.

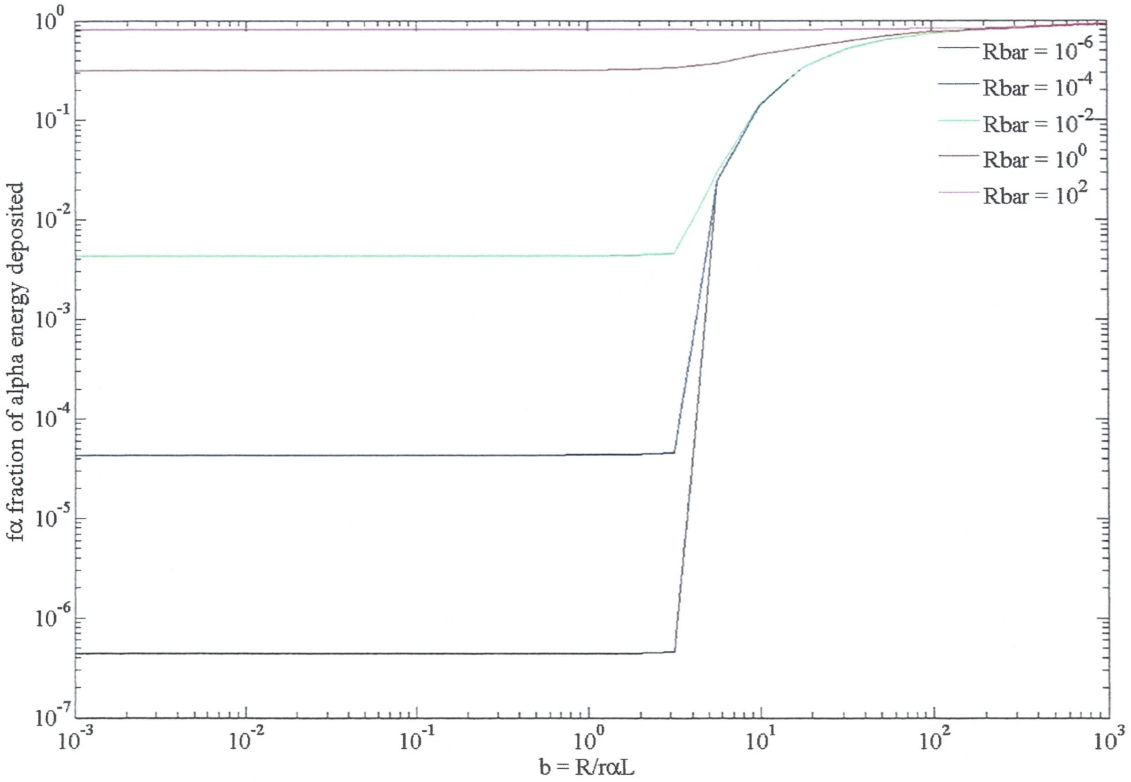

Figure 3.3 b vs f_α at different values of $\bar{R}$ for an elongation of 0.5.

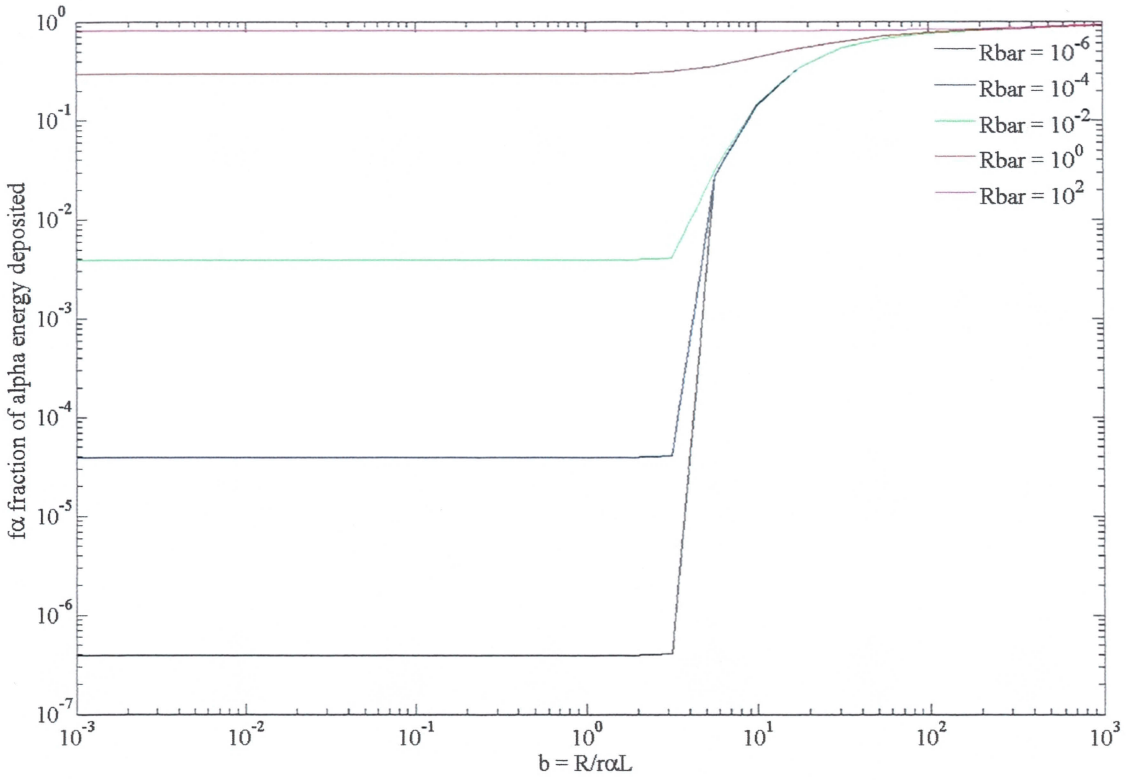

Figure 3.4 b vs f_α at different values of $\bar{R}$ for an elongation of 1.

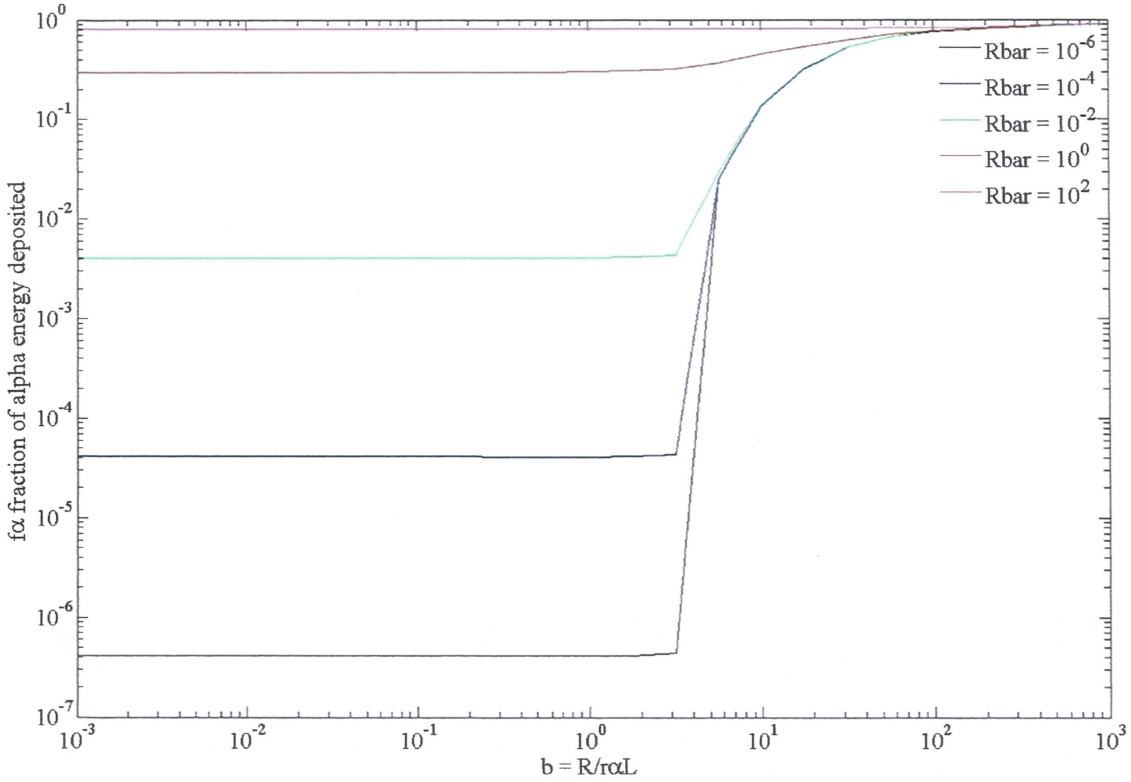

Figure 3.5 b vs f_α at different values of $\bar{R}$ for an elongation of 2.

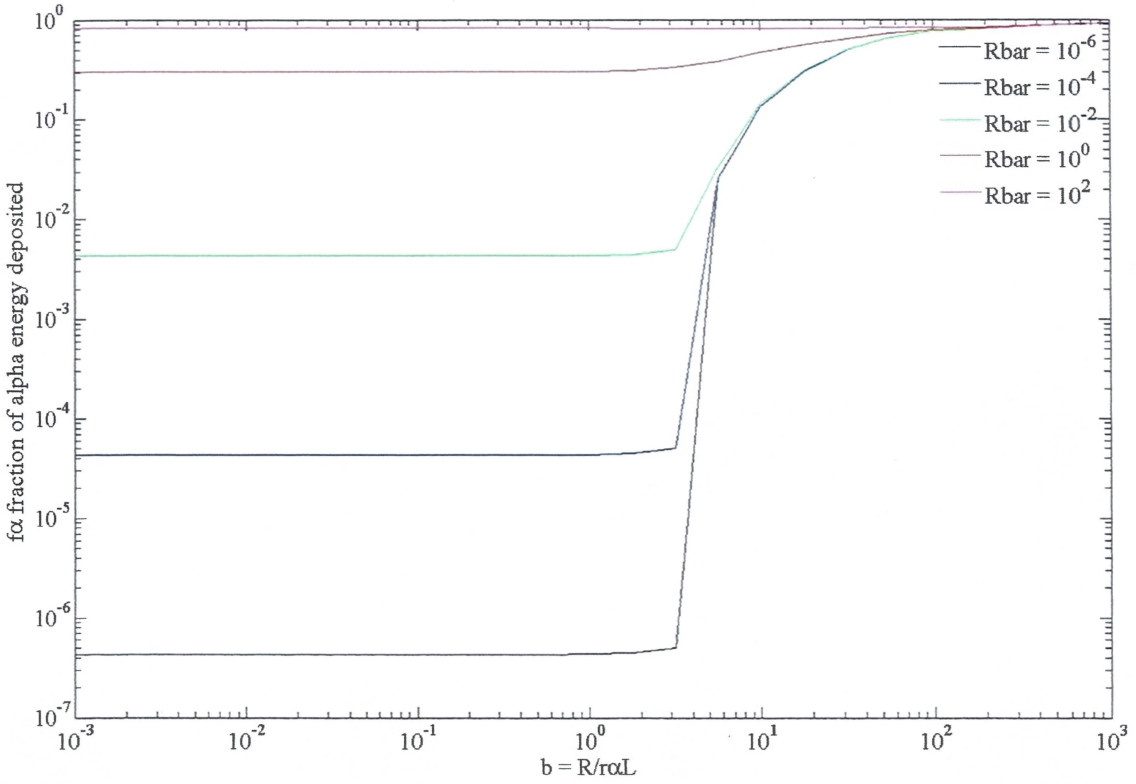

Figure 3.6 b vs f_α at different values of $\bar{R}$ for an elongation of 5.

In the low magnetic field limit (b≪1), the alpha deposition is $\sim\frac{2}{5}\bar{R}$ for $\bar{R} \le 1$. This is *lower* than the Basko and Kemp [3] result of $\frac{8}{3}\bar{R}$ for an infinite cylinder with axial magnetic field, which is expected if for no other reason than because of finite end effects. For higher densities $(\bar{R} > 1)$, the deposition asymptotically approaches 1.0. Effects of magnetic field on deposition are not observed until b~2, since the path length of an alpha particle is not significantly altered unless it is trapped on a field line. Once there are roughly 4 alpha Larmor radii in the target, the deposition rises sharply with magnetic field, Figure 3.3. At b~10, the curves of constant $\bar{R}$ begin to coalesce,

indicating that the deposition becomes independent of density for high magnetic fields. For b>100, the deposition is essentially independent of density, with the value asymptotically approaching 1.0.

3.2.2. Curve Fit and Limiting Cases

The alpha deposition results can be utilized to help make MIF ignition calculations. However, it is more convenient to produce a curve fit for the data. Using our numerical results, we came up with the following expression which approximates the alpha deposition for FRC's:

$$f_\alpha = \frac{x + x^2}{1 + 3x^{4/3} + x^2}, \tag{3.5}$$

where

$$x = 0.4\bar{R} + 0.076e^{2\log \bar{R}^2} + e^{-\frac{1}{(b/7)^{10}}}\left(\frac{b}{4}e^{-\frac{25^2}{b^2}} + 200e^{-\frac{\log(b/5.6)^2}{2(0.066)^2}}\right) + 2.5e^{-\frac{\log \bar{R}^2}{9^2}}e^{-\frac{\log(b/30)^2}{2\times(0.36)^2}}. \tag{3.6}$$

This curve is accurate to within ±4% for b<2 and b>15, and it is within ±15% for the 2<b<15 interval, where the deposition rises sharply with b. The form of Equation (3.5) was inspired by the curve fit offered by Basko and Kemp [3] for cylindrical targets. Equation (3.6) was determined through trial and error, but consists of superposition and/or multiplication of the four following functions:

Density Function $0.4\bar{R} + 0.076e^{2\log \bar{R}^2}$

Magnetic Function $\left(\frac{b}{4}e^{-\frac{25^2}{b^2}} + 200e^{-\frac{\log(b/5.6)^2}{2(0.066)^2}}\right)$

Coupling Function $2.5e^{-\frac{\log \bar{R}^2}{9^2}}e^{-\frac{\log(b/30)^2}{2\times(0.36)^2}}$

Switch Function $e^{-\frac{1}{(b/7)^{10}}}$

The density function captures the effects of density in the low magnetic field limit ($b \ll 1$). The magnetic function captures the effects of the magnetic field when the deposition results become independent of density ($b \gg 1$). The intermediate region where both density and magnetic are important is approximated with the product of the switch function and the coupling function. The switch function turns the coupling function on at b~5 and varies from 0 to 1.0 over a very short range of b. We use this curve fit in Chapter 4 in the calculation of fusion heating power and to plot Lindl-Widner diagrams.

CHAPTER 4

LINDL-WIDNER DIAGRAMS

Thermonuclear ignition of the FRC occurs when the heating power exceeds the radiative and thermal conduction losses. This condition is determined by a power balance. For inertial fusion systems, including ICF and MIF, the ignition region is typically plotted in the ρR-T parametric plane, where ρR is the product of the mass density and target radius, denoted 'aerial density'. The choice of ρR is not arbitrary. Confinement for inertial targets requires that the confinement time exceeds the time required to burn a fraction ξ of the fusion fuel, leading to the result

$$\rho R > \frac{2 m_i v_{therm}}{<\sigma v>_{DT}} \left(\frac{\xi}{1-\xi} \right), \tag{4.1}$$

where m_i is the average mass of an ion, v_{therm} is the expansion velocity of the target, and $<\sigma v>_{DT}$ is the DT fusion cross section at some temperature, typically evaluated at 10 keV. Further discussions on the topic of inertial confinement can be found in, for example, Reference [37]. Lindl [18] discussed the physics of DT ICF capsules using ρR-T diagrams. Following Reference [34], all ρR-T diagrams are called

Lindl-Widner (LW) diagrams. Kirkpatrick [32] for the first time used L-W diagrams to study the parameter space for MIF. The targets were assumed to have a uniform magnetic field. We have extended Kirkpatrick's work to include alpha deposition, using our results from Chapter 3. To date, no one has performed such a calculation accounting for a realistic magnetic field topology.

4.1. Power Balance Equation

Lindl-Widner diagrams represent the *dE/dt=0* contour in ρR-T parameter space showing the region of fusion ignition. Inside this contour, the target with the state and scale determined by ρR-T will result in a net increase in energy due to the heating power. The power balance equation for a burning thermonuclear target is [32]

$$\frac{dE}{dt} = P\frac{dV}{dt} + f_{\alpha} Q n^2 \langle \sigma \upsilon \rangle V - P_{brems} - P_{sync} - Ak\nabla T, \tag{4.2}$$

where P is the pressure, V is the target volume, Q is the fusion reaction energy, n is the particle number density, $\langle \sigma \upsilon \rangle$ is the velocity averaged cross section for the fusion reaction, A is the target surface area, k is the thermal conductivity, and T is the temperature. P_{brems} represents Bremsstrahlung radiation loss given by

$$P_{brems} = 1.44e^{-40} n^2 T^{\frac{1}{2}} V \tag{4.3}$$

and P_{sync} represents synchrotron radiation loss given by

$$P_{sync} = 5.342e^{-24} nB^2 T(1 + \frac{T}{2.367e^9})V. \tag{4.4}$$

The first term (PdV/dt) in Equation (4.2) represents the work done by the compression

of the liner on the target. The second term is the power from fusion reactions. The last term is the thermal conduction loss.

The contours for ρR vs T space are generated using (4.2) with a Matlab code. We calculated the ignition region for constant values of b. We chose b as our independent parameter since increasing $\bar{R}$ would require impractically high densities before significant fusion heating power could be observed. The compressional heating is not included in the calculation. Thus, we are computing ignition curves at the point of stagnation, after the liner has transferred as much kinetic energy as possible to the target. There are two merits to setting compressional work to zero. First, it allows one to isolate the capability of the fusion heating power. Second, it determines the region that the target needs to intersect during the implosion. The L-W results are discussed in the following section.

4.2. Results

Regions of positive ignition are represented as dE/dT=0 contours, and are plotted in the ρR-T plane for contours generated at constant b. We found that there is a critical value of b (6.07) below which there is no net heating power, Figure 4.1. In this low range, the ignition region grows rapidly with b since the fractional deposition increases rapidly as shown in Figure 3.3.

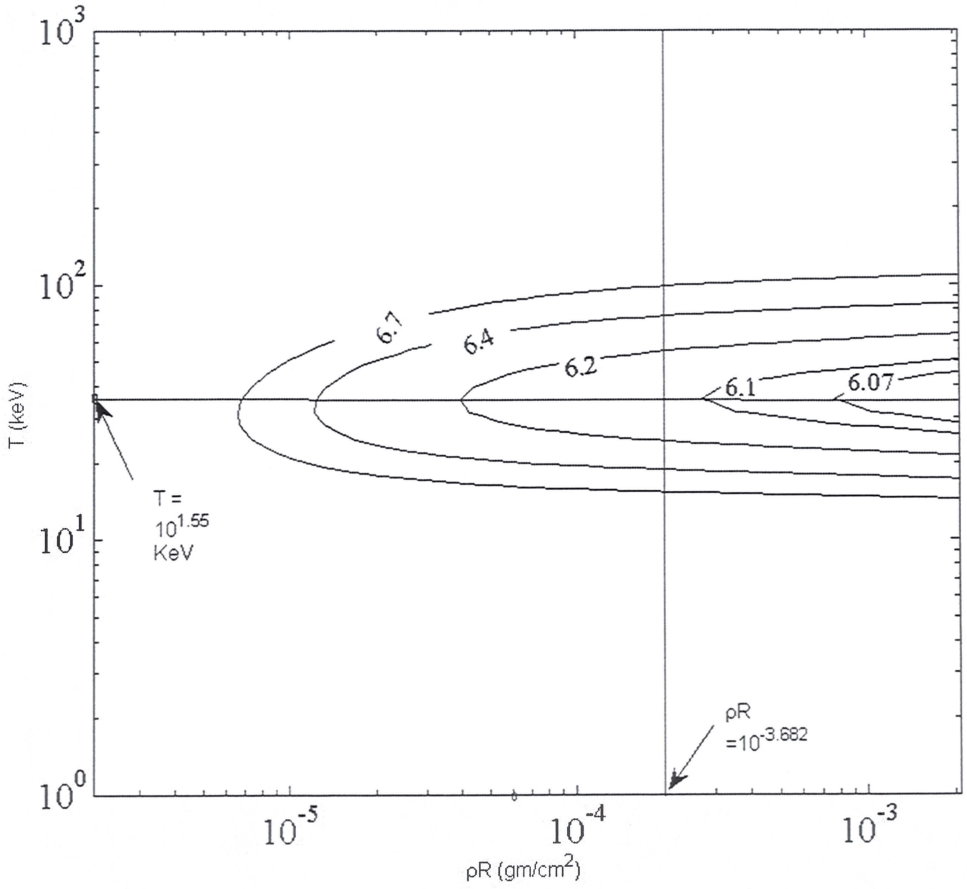

Figure 4.1 Regions of positive target heating for b<7. Powers are calculated at the horizontal and vertical lines shown to illustrate the partitioning of powers (heating/losses).

It is of interest to determine the dominant loss mechanism(s) to see what affects the ignition boundary. To do so, we can compare the heating and loss powers along constant data lines which intersect the ignition contour. We chose to plot the powers along the horizontal and vertical lines drawn in Figure 4.1, using b=6.7. The results are powers vs. aerial density at T=35.5 keV, Figure 4.2, and powers vs. temperature at

$\rho R=2.08\times10^{-4}$ gm/cm^2, Figure 4.3. The fusion heating power, Bremsstrahlung radiation loss, and thermal conduction are proportional to n^2 and therefore follow the same trend. At 35.5 keV, the fusion heating power dominates these loss mechanisms. P_{sync} intersects the other power curves since it is proportional to n, and dominates the fusion heating power at $\rho R<10^{-5}$ gm/cm^2, Figure 4.2.

We extracted the heating power and radiative and thermal conduction powers are plotted along the horizontal and vertical (We chose a random set of parameters ρR and T from the positive gain region in Figure 4.1 to plot individual powers. Figure 4.2 is the plot of aerial density ρR vs. individual power at constant temperature of 35.5 keV. It can be observed from Figure 4.2 that fusion power increases with increasing aerial density. Synchrotron radiation loss dominates the fusion power at lower densities.

Figure 4.3 is a comparison of the fusion heating powers and losses vs. temperature for $\rho R=2.08\times10^{-4}$ gm/cm^2. Fusion heating power has a maximum near 100 keV, corresponding to the peak reaction rate as a function of temperature. Synchrotron radiation dominates the other losses mechanisms. Thus, in consideration of Figure 4.2 and Figure 4.3, it appears that the energy loss in the target is primarily determined by synchrotron radiation, and the balance between it and the fusion heating power essentially determines the ignition region.

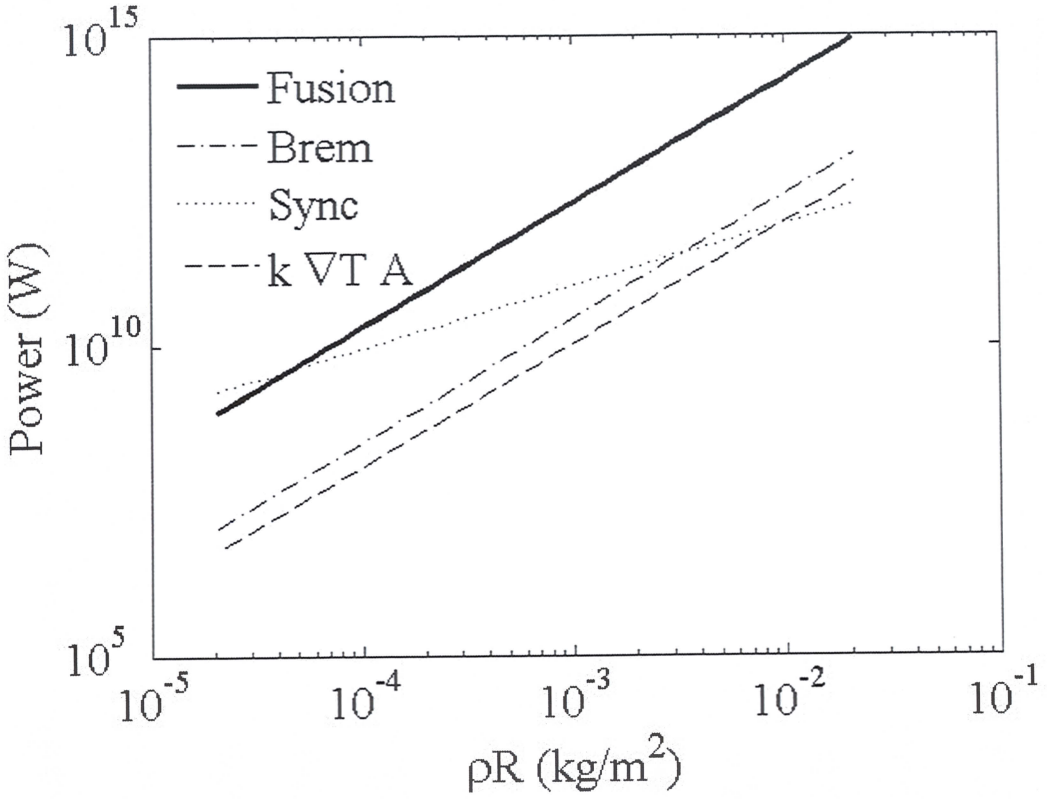

Figure 4.2 Comparison of fusion heating power, Bremsstrahlung radiation, synchrotron radiation, and thermal conduction vs. ρR for T = 35.5 keV (The powers correspond to data extracted along horizontal line as shown in Figure 4.1).

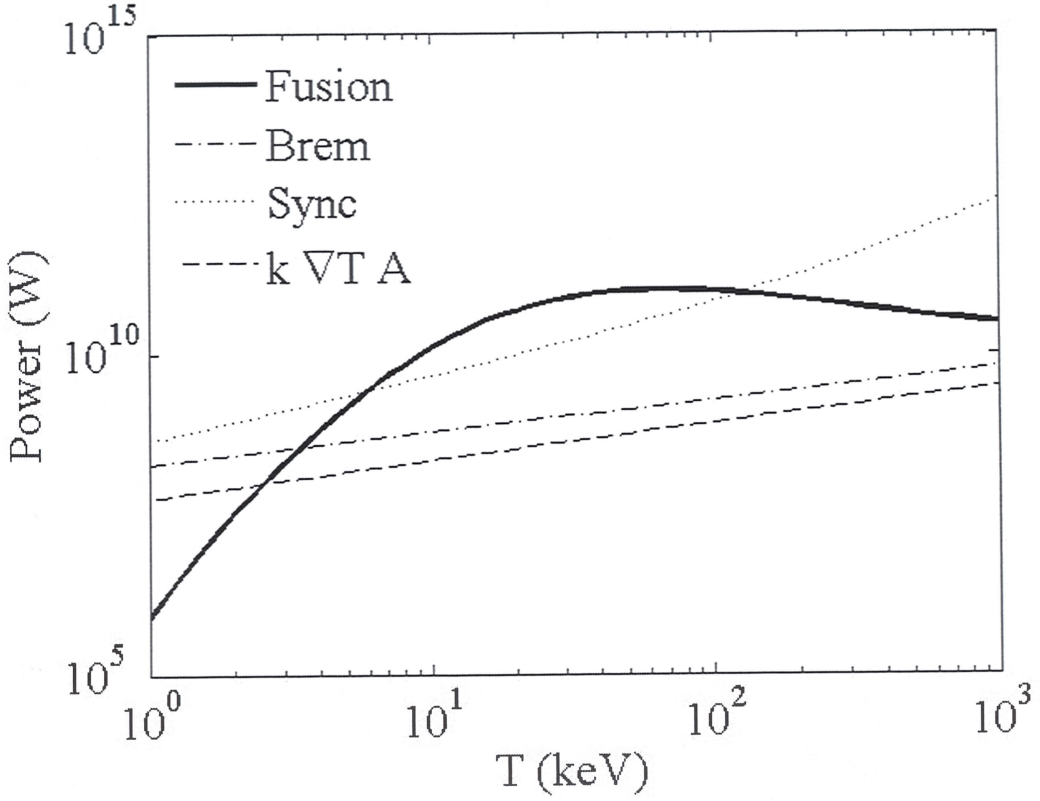

Figure 4.3 Comparison of fusion heating power, Bremsstrahlung radiation, synchrotron radiation, and thermal conduction vs. temperature for $\rho R = 2.08\times10^{-4}$ g/cm^2. (The powers correspond to data extracted along vertical line as shown in Figure 4.1).

Figure 3.3 shows that the rate of change of f_α with b decreases significantly for b>10 as fa→1.0. Additionally, the synchrotron radiation power is proportional to B^2, Equation. (4.4). These two factors cause the ignition region to retreat to higher ρR as b is increased beyond 20, Figure 4.4.

From these results, a 'sweet spot' which maximizes target ignition can be found with 10<b<20, a temperature of ~30 keV, and a $\rho R > 10^{-5}$ g/cm^2. In order to provide a

sense of scale, we can pick a typical value for the density expected at peak compression, and that fixes the scale for R and B. Assuming a number density for a DT plasma of 10^{25} m^{-3}, this corresponds to a 2.5 cm target with a magnetic field strength of 172 T.

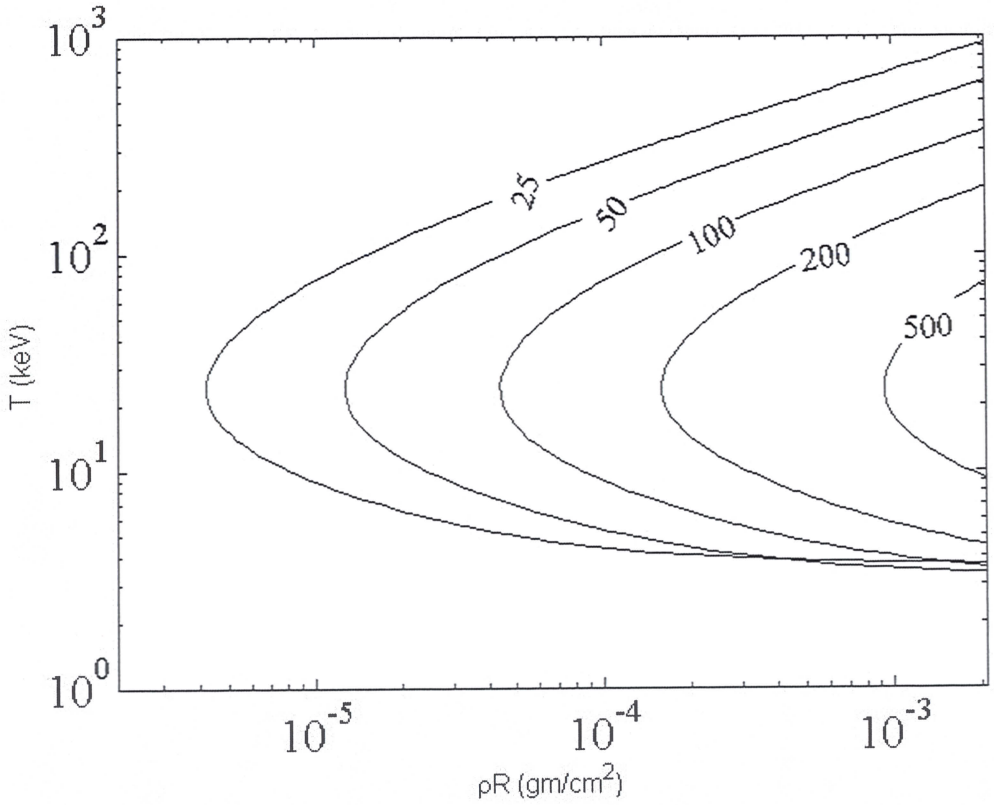

Figure 4.4 Regions of positive target heating for b>20.

CHAPTER 5

CONCLUSIONS

Magnetoinertial fusion (MIF) is emerging as a prominent fusion confinement concept for terrestrial power and propulsion applications. In this approach, a liner compresses a magnetized target to thermonuclear ignition. The field reversed configuration (FRC), a compact toroid with no toroidal magnetic field, has become the leading candidate for the target in MIF plasmas. Ignition of MIF targets requires the fusion heating power to exceed the thermal and radiative losses. One of the primary challenges is calculating the fusion heating power, which must be accomplished through scattering collisions between the charged particle fusion products and the background plasma. In a burning DT plasma, this corresponds to 3.5 MeV alpha ($^4_2\mathrm{He}$) ions. The scattering of alpha particles occurs over a scale length typically much longer than the FRC radius, and since the FRC has a complex topology, simple, comprehensive, analytic models accounting for the field curvature and gradients have not been derived.

We developed a particle model to calculate alpha deposition for FRC targets. The numerical model solves the equations of motion for alpha particles traveling in a cylindrical FRC target. The numerical results show that the fractional deposition from the 4D parameter space (density, magnetic field, target radius, and elongation) can be collapsed to a family of 2D curves as a function of two dimensionless variables,

b and $\bar{R}$, following the work of others [3]. b is the ratio of the target radius to the alpha Larmor radius, and it is proportional to the magnetic field. $\bar{R}$ is the ratio of the target radius to the mean free path, and it is proportional to density.

When plotted vs. b with curves of constant $\bar{R}$, alpha deposition was found to be independent of elongation. In the low magnetic field limit (Larmor radius≫target radius), the deposition was linear with density until the collision mean free path approached the target radius. For very high densities, the fractional deposition asymptotically approaches 1.0. In the high magnetic field limit (Larmor radius ≪ target radius), the fractional deposition is independent of density and again asymptotically approaches 1.0. In the intermediate magnetic field regime, where the Larmor radius is of the same order as the target radius, density and magnetic field both play a role in the fractional deposition. The fractional deposition rises sharply with the magnetic field from the low density limit, as some particles become trapped by the FRC. We were able to determine a curve fit to the deposition which was accurate to within 4% for both the low and high magnetic field regimes, and within 15% for the intermediate magnetic field regime.

Having a model for alpha deposition allows us to calculate fusion heating power and ignition criteria while accounting for the FRC magnetic field topology. Lindl-Widner diagrams are contours in the ρR-T plane which represent the boundary between net heating and cooling in an inertial target. In our model, the power balance equation to compute these diagrams accounts for alpha deposition heating power, Bremsstrahlung radiation, synchrotron radiation, and thermal conduction.

Using these plots we studied the effects of b on the ignition region. Qualitatively, the ignition region appears as a left pointing finger centered at ~35 keV in the ρR-T space. For low values of b, the ignition region is negligible until b>6. The region grows rapidly with b, protruding to smaller ρR, until b~10. The region does not change significantly until b>20, upon which it begins retreating to higher ρR.

The boundary separating net heating from cooling (ignition region) appears to be determined by the balance between synchrotron radiation and the alpha deposition heating power. The 'sweet spot' appears to be for FRC targets defined by $10<b<20$, a temperature of ~30 keV, and a $\rho R>10^{-5}$ g/cm^2. If we pick a typical density for compressed DT targets (10^{25} m^{-3}), this corresponds to a 2.5 cm target with a magnetic field strength of 172 T.

This study presents the first alpha deposition model for FRC targets in magnetoinertial fusion. Our model can be used as a basis for further development of deposition models for other closed field topologies. Additional insights can be gained with further exploration of the ignition space with Lindl-Widner diagrams using our alpha deposition model.

REFERENCES

[1] Thompson, S., Cassibry, J., Kirkpatrick R., *Parameter Space for Plasma Liner Driven Magnetoinertial Fusion.* American Physical Society, 48th Annual Meeting of the Division of Plasma Physics, October 30-November 3, 2006.

[2] Tuszewski, *Field Reversed Configurations.* Nuclear Fusion, 1988. **28**(11): p. 2033-EOA.

[3] Basko, M.M., Kemp, A.J., Meyer-ter-Vehn, J., *Ignition Conditions for Magnetized Target Fusion in Cylindrical Geometry.* Nuclear Fusion, 2000. **40**(1): p. 59-68.

[4] Artsimovich, L.A., *Research on Controlled Nuclear Fusion and the Physics of High-Temperature Plasma in the USSR.* J. Nucl. Energy, Part C Plasma Phys., 1965. **7**: p. 477-489.

[5] Lindle, J., *Development of Indirect Drive Approach to Inertial Confinement Fusion and the Target Physics Basis for Ignition and Gain.* Phys. Of Plasmas, November 1995. **2**(11).

[6] Ribe, F.L., *Fusion Reactor Systems.* Review of Modern Physics, 1975. **47**(1): p. 7-48.

[7] Fujita, T., et al., *Plasma Equilibrium and Confinement in a Tokamak with Nearly Zero Central Current Density in JT-60U.* Physical Review Letters, 2001. **87**(24).

[8] Hazeltine, R.D., Meiss, J.D., *Plasma Confinement*, ed. P. David. 1991.

[9] Kirkpatrick, R.C., Lindemuth, I. R., *Magnetized Target Fusion: An Overview of the Concept. in Current Trends in International Fusion Research.* Panarella, Plenum Press, 1997.

[10] Cassibry, J., et al., *Numerical Modeling of a Pulsed Electromagnetic Plasma Thruster Experiment.* Journal of Propulsion and Power, 2006. **22**(2): p. 628-636.

[11] Thompson, S., *Lindle-Widner Diagrams for Plasma Liner Driven Magneto-Inertial Fusion.* Master's thesis, 2007

[12] Thio, Y.C.F., et al., *Magnetized Target Fusion in a Spheroidal Geometry With Standoff Drivers in Current Trends in International Fusion Research -- Proceedings of the Second Symposium.* Ottawa, Canada: NRC Research Press, 1999.

[13] Siemon, R.E., Lindemuth, I.R., Schoenberg, K.F., *Why Magnetized Target Fusion Offers a Low-Cost Development Path for Fusion Energy.* Comments on Plasma Physics and Controlled Fusion, 1999. **18**: p. 363.

[14] Intrator T., et al., *A High Density Field Reversed Configuration (FRC) Target for Magnetized Target Fusion: First Internal Profile Measurements of a High Density FRC.* Phys. Of Plasmas, 2004. **11**(5): p. 5.

[15] Degnan, J.H., et al., *Compression of Plasma to Megabar Range Using Imploding Liner.* Physical Review Letter, 1999. **82**(13).

[16] Bauer, B., et al., *A Community White Paper on Magnetized High Energy Density Laboratory Plasmas.* 2007.

[17] Thio, Y.C.F., et al., *Plasma Liner Formation Physics Exploratory Experiment.* 2001.

[18] Lindle, J.D., *Introduction To the Physics ICF Capsules in Inertial Confinement Fusion Course and Workshop.* 1988.

[19] Kirkpatrick, R.C., Smitherman, D.P., *DT Alpha Energy Deposition in a Magnetized Plasma.*

[20] Kirkpatrick, R.C., *Field Gradient Dependence for Fusion Self-Heating in MTF Targets*, Los Alamos National Labs. p. 15.

[21] Degnan, J.H., et al., *Compact Toroid Formation, Compression, and Acceleration.* Physics of Fluids B, 1993. **5**(8): p. 2938-2958.

[22] Monkhorst, H.J., Rostoker N., *Controlled Fusion in Field Reversed Configuration and Direct Energy Conversion*. 2007, Regents of the University of California, Oakland, CA (US), University of Florida Research Foundation, Gainsville, Fl(US): USA.

[23] Barnes, D.C., et al., *Field Reversed Configuration (FRC) Equilibrium and Stability*, in *19th Fusion Energy Conference* 2002: Lyon, France.

[24] Steinhauer, L.C., *Recent Advances in FRC Physics.* Fusion Engineering, 1995. SOFE '95. 'Seeking a New Energy Era', 16th IEEE/NPSS Symposium, 1995. **2**: p. 1407-1412.

[25] Wright, J.K., Medford, R. D., et al., *Equilibrium Configuration of the Plasma in Theta Discharges with Reversed Trapped Magnetic Fields.* Journal of Nuclear Energy Part C 1961. **3**(3): p. 242-245.

[26] Kadish, A., *Elongated Field-Reversed Plasma Equilibria.* Physics of Fluids, 1979. **22**(11): p. 2248-2249.

[27] Solov'ev, L.S., *Hydromagnetic Stability of Closed Plasma Configurations.* Reviews of Plasma Physics, New York City, New York, Consultants Bureau, 1975. **6**: p. 239.

[28] Cohen, S.A., *Maintaining the Closed Magnetic-Field-Line Topology of a Field-Reversed Configuration with the Addition of Static Transverse Magnetic Fields.* Physics of Plasmas, 2000. **7**(6): p. 2539-2545.

[29] Goldston, R.J., Rutherford, P.H., *Introduction to Plasma Physics*. 1997, Bristol and Philadelphia: Institute of Physics Publishing.

[30] Jahn, R.G., *Physics of Electric Propulsion.* 1968: McGraw-Hill. 339.

[31] Goldston, R.J., Rutherford, P.H., *Introduction to Plasma Physics*. 1995, London: Institute of Physics Publishing. 491.

[32] Kirkpatrick, R.C., Lindemuth, I.R., Ward, M.S., *Magnetized Target Fusion: An Overview.* Fusion Technology, 1994. **27**: p. 201-214.

[33] Shampine, M.W.R., *The Matlab ODE Suite.* SIAM Journal on Scientific Computing, 1997. **18**: p. 1-22.

[34] Thio, Y.C.F., et al., *A Physics Exploratory Experiment on Plasma Liner Formation.* J. Fusion Energy, 2001. **20**(1/2): p. 1-11.

[35] Atzeni, S., Meyer-Ter-Vehn, J., *The Physics of Inertial Fusion: Beam Plasma Interaction, Hydrodynamics, Hot Dense Matter.* 2004, Oxford, Oxford Science Publications.